‖ Nanomaterials │*Hot Paper*│

Magnetic N-Enriched Fe$_3$C/Graphitic Carbon instead of Pt as an Electrocatalyst for the Oxygen Reduction Reaction

Xiaobai Wang, Peng Zhang, Wei Wang, Xiang Lei, and Hua Yang*[a]

Abstract: A series of Fe$_3$C/C-N$_x$ nanoparticles (NPs) with different nitrogen content are prepared by a simple one-pot route. In the synthetic procedure, aniline and acetonitrile are simultaneously used as the carbon and nitrogen source. The effect of calcination temperature on the structural and functional properties of the materials is investigated. Magnetic measurement shows that the sample prepared at 800 °C (Fe$_3$C/C-N$_{800}$ NPs) possesses the highest M_s value of 77.2 emu g^{-1}. On testing as oxygen reduction reaction (ORR) catalysts, the sample prepared at 750 °C (Fe$_3$C/C-N$_{750}$ NPs) shows the best ORR performance among the series, with a more positive onset potential (+0.99 V vs. RHE), higher selectivity (number of electron transfer n ≈ 3.93), longer durability, and stronger tolerance against methanol crossover than commercial Pt/C catalysts in a 0.1 M KOH solution. Moreover, in acidic solution, the excellent ORR activity and stability are also exhibited.

Introduction

Highly active and durable catalysts for the ORR are of great significance for large scale application of fuel cells.[1] The state-of-the-art catalysts are Pt-based materials,[2] however, they still suffer from several serious problems, including prohibitive cost,[3] limited availability, poor durability, and the issue of methanol crossover;[4] these obstacles hamper the commercialization of this technology. Thus, the exploration of highly active non-platinum metal catalysts (NPMCs) for the four electron ORR with comparable electrochemical performance is a paramount subject for fuel cells.[5]

Considering the harsh ORR conditions, it has been found that only a few types of materials are active and durable, such as carbon-accompanied transition metal–nitrogen composites (M–N–C, with M = Fe, Co, etc.),[6] metal-free N-doped carbon materials,[7] and transition metal–carbon materials,[8] and so on. Among the best is the M–N–C catalyst in which the active sites are believed to involve surface nitrogen coordinated with metals.[5b]

Very recently, researchers reported a new type of NPMC based on Fe$_3$C that was active towards ORR. Hou et al. fabricated N-doped Fe/Fe$_3$C@C nanoboxes supported on reduced graphene oxide sheets as ORR catalysts in alkaline media.[9] Yang et al. found that the N-doped bamboo-like carbon nanotube/Fe$_3$C nanoparticles (NPs) exhibited excellent ORR activities in both alkaline and acidic media.[10] Though interesting, limited information is known about the role of the Fe$_3$C phase in catal-

ysis, probably owing to two main aspects: 1) The morphology of the catalysts is very important; as in Hou and Yang's example,[9–10] only the regular shaped catalysts can exhibit excellent ORR activities; 2) it has been found that the prepared Fe$_3$C-based catalysts contained a certain amount of surface nitrogen atoms, suggesting the possible presence of Fe-N$_x$ or/and C-N$_x$ moieties, and the Fe-N$_x$ and C-N$_x$ moieties are probably active towards ORR.[11] More exactly, the nitrogen-induced charge delocalization can facilitate the bridge model chemisorption of O$_2$ on the N-doped Fe$_3$C catalysts, which can effectively weaken the O—O bonding to promote the ORR.[12]

For the present view, the selectivity of oxygen reduction is quite important, that is, the four electron reaction or two electron reaction. As in Liu's example, non-N-doped carbon generated about 80% H$_2$O and 20% H$_2$O$_2$.[13] However, the formation of H$_2$O$_2$ is undesirable because it reduces the effective cathodic current, contaminates the surroundings of the catalyst, and corrodes the polymer membrane present in fuel cells. On the other hand, N-doped carbon generated more than 96% H$_2$O and less than 4% H$_2$O$_2$, which means that doping nitrogen on carbon is not only favorable for the ORR activity, but also improves the selectivity towards oxygen reduction. Within this context, it is extremely important to maximize the nitrogen content in the ORR catalysts so that they exhibit the best ORR activity. However, most of the current synthetic routes to produce ORR catalysts are complicated and the nitrogen content and morphology are uncontrollable. This presents a highly important and urgent problem that needs to be solved.

In this paper, we firstly report a simple one-pot route to synthesize Fe$_3$C NPs encased by uniform graphitic shells by directly calcining the matrix of ferric chloride, aniline, and acetonitrile under nitrogen. By varying the calcination temperatures, a series of materials with different nitrogen contents (hereafter referred to as Fe$_3$C/C-N$_x$, in which x is the calcination tempera-

[a] X. Wang, P. Zhang, W. Wang, X. Lei, Prof. Dr. H. Yang
College of Chemistry, Jilin University
Changchun, 130012 (P.R. China)
E-mail: huayang86@sina.com

⬚ Supporting information for this article is available on the WWW under
http://dx.doi.org/10.1002/chem.201505138.

ture) are obtained. Magnetic measurements reveal that all of the as-synthesized $Fe_3C/C-N_x$ NPs display soft magnetic behavior at room temperature. On testing as ORR catalysts, the $Fe_3C/C-N_x$ NPs exhibit excellent activities and stabilities in alkaline media.

Results and Discussion

Structure and morphology

Figure 1a shows the XRD patterns of the four kinds of $Fe_3C/C-N_x$ ($x = 650, 700, 750, 800\,°C$) NPs. All of the diffraction peaks are in good agreement with that of the Fe_3C (JCPDS card no. 89-2867). The nanosized nature of the $Fe_3C/C-N_x$ samples can

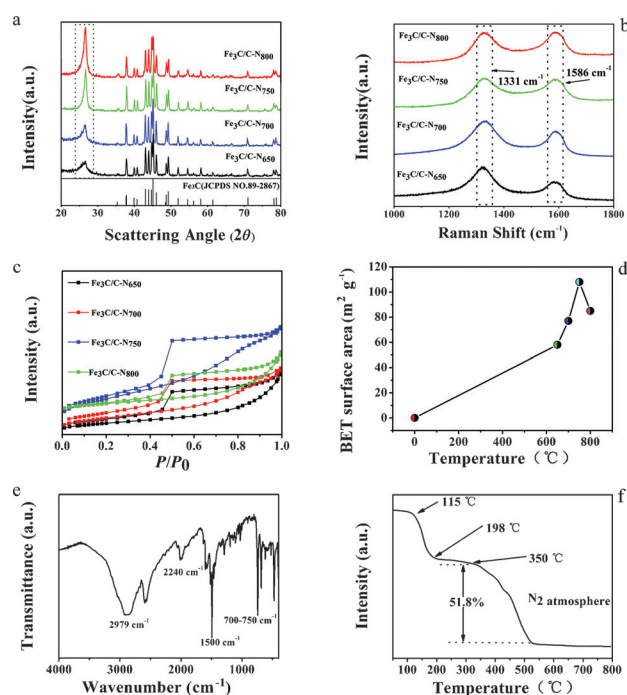**Figure 1.** a) XRD patterns; b) Raman spectra; c) N_2 sorption isotherm; and d) BET surface areas of the as-synthesized $Fe_3C/C-N_x$ ($x = 650, 700, 750, 800\,°C$) NPs; e) FTIR spectrum; and f) TGA curve of $Fe_3C/C-N_x$ precursor.

be deduced from these strong and broaden peaks. A sharp peak appearing $2\theta = 26.5\,°$ is ascribed to a crystalline structure of carbon (JCPDS card no. 26-1079). Note that by increasing the pyrolysis temperature from 650 to $800\,°C$, this peak is enhanced. This enhancement may be because the high temperature provides enough energy to promote the formation of crystalline carbon (here we refer to graphitic carbon). Raman spectra are used to support this view. As can be seen in Figure 1b, the G-band for graphitic carbon appears at about $1586\,cm^{-1}$ and the D-band for amorphous carbon[14] locates at about $1331\,cm^{-1}$. Typically, the relative intensity ratio of the D-band to the G-band (I_D/I_G) reveals the degree of graphitization of samples. The values for the four kinds of $Fe_3C/C-N_x$ NPs are 2.52, 1.97, 1.05, and 0.97, respectively. Among the series, $Fe_3C/C-N_{800}$ NPs has the lowest (I_D/I_G) value and so it has the highest

degree of graphitization, confirming that the high temperature is the key factor in the formation of graphite carbon. This result is consistent with the XRD analysis. The degree of graphitization relates closely to the ORR performance and magnetic parameters of the materials.[10, 15]

Figure 1c depicts the N_2 adsorption/desorption isotherm of the four kinds of $Fe_3C/C-N_x$ NPs. All samples exhibit type IV isotherms with hysteresis loops, signifying that the samples possess micro- and mesopores.[16] The unrestricted adsorption is confirmed by the hysteresis loop in the high-pressure regime and the increase gas uptake at $P/P_0 > 0.90$ suggests that there are slit-like and bottle-like pores in the samples. The specific surface areas calculated from Brunauer–Emmet–Teller (BET) are 59, 77, 110, and $86\,m^2\,g^{-1}$, for the four kinds of $Fe_3C/C-N_x$ NPs, respectively, as shown in Figure 1d. One can see that with increasing the pyrolysis temperature, the specific surface area is increased. However, comparing with the $Fe_3C/C-N_{750}$ NPs, the specific surface area for $Fe_3C/C-N_{800}$ NPs is decreased, indicating that the high temperature likely leads to the collapse of the mesopores. In other words, the specific surface area reaches the maximum when the sample is prepared at $750\,°C$.

To investigate the formation mechanism of the $Fe_3C/C-N_x$ NPs, FTIR and TGA are performed to analyze the precursor of $Fe_3C/C-N_x$ NPs. Figure 1e shows the FTIR spectrum of the precursor in the $400–4000\,cm^{-1}$ region. The $1300–1500\,cm^{-1}$ region is ascribed to the saturated C−H deformation vibration. The presence of the bands at 2240 and $2979\,cm^{-1}$ are the characteristic of the C−N and C−H stretching vibrations.[17] The existence of these bands confirms that there is acetonitrile in the precursor. Then, the relative weakness of the band at $700–750\,cm^{-1}$ is indexed to the vibration of mono-substituted benzene. In addition, the ring stretch of quinoid and benzenoid forms is observed at 1580 and $1500\,cm^{-1}$.[18] These observations confirm that the existence of aniline. Note that there are no peaks for ferrite or other iron-containing phase, signifying that the iron should exist in ionic condition. Finally, due to the oxidation of aniline, there may be nitrobenzene or quinoid and so on in the precursor.

Figure 1e shows TGA curve for the precursor of $Fe_3C/C-N_x$ NPs measured in a N_2 atmosphere. There are four major steps of weight loss. The initial weight loss starts at below $198\,°C$ is likely due to the vaporization of bound water. The second weight loss is very small, starting from 198 to $350\,°C$. This is the decomposition temperature range of nitrobenzene, quinoid, and oligomers of aniline in a N_2 atmosphere. It seems a reasonable deduction that part of these organics will be decomposed in this temperature range. The third weight loss of 51.8% starts at $350\,°C$ and ends at around $530\,°C$, which is most probably due to three important reasons: 1) The decomposition of organics.[19] 2) The nucleation of Fe_3C, and 3) The evaporation of $FeCl_3$.[20] Finally, the fourth weight loss is not very obvious at 1.8% between 530 and $800\,°C$, which is likely due to the decomposition of some organic byproducts.

The morphology of $Fe_3C/C-N_{750}$ NPs is investigated by TEM and HRTEM. As shown in Figure 2a, the $Fe_3C/C-N_{750}$ NPs are embedded in a sheet-like carbon. There is a $Fe_3C/C-N_{750}$ particle with core-shell structure in the circle region. Figure 2b rep-

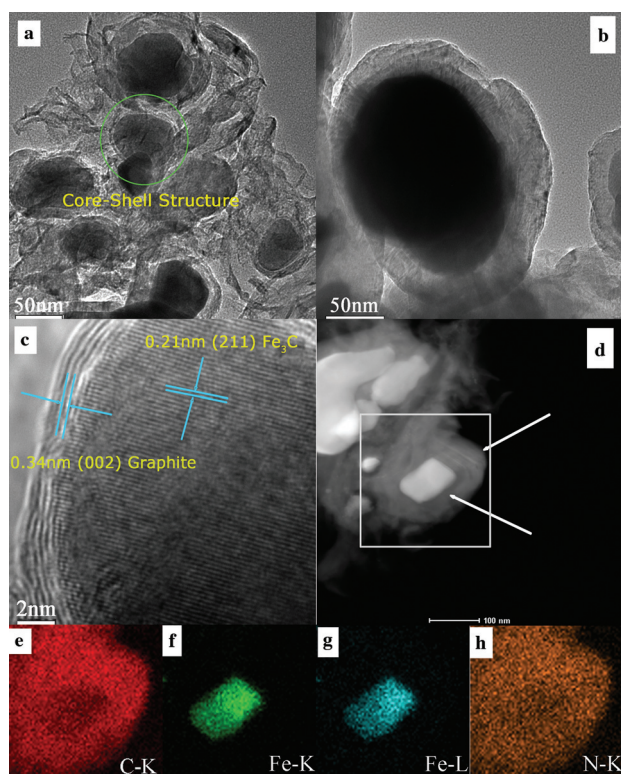into Fe and nitrogen-rich carbon matrix (Fe is surrounded by the nitrogen-rich carbon matrix). When the temperature reaches the crystallization point of Fe_3C, the surrounding nitrogen-rich carbon matrix will play the role of carbon source to react with Fe to form Fe_3C; In turn, the Fe_3C will play the role of catalyst to change the surrounding carbon matrix into graphite carbon. With the increase of pyrolysis temperature, the degree of graphitization of samples is increased. This has been demonstrated by the XRD and Raman analysis. In addition, there is a certain amount of surface nitrogen that has been demonstrated by the elemental mapping result, which most probably exists in the form of $Fe-N_x$ or/and $C-N_x$ moieties.

The low-resolution XPS spectra for the as-synthesized $Fe_3C/C-N_x$ NPs are shown in Figure 3a and Figure S1a (the Supporting Information). One can see that there are C 1s, N 1s, O 1s, and Fe 2p in the spectra, confirming that the existence of
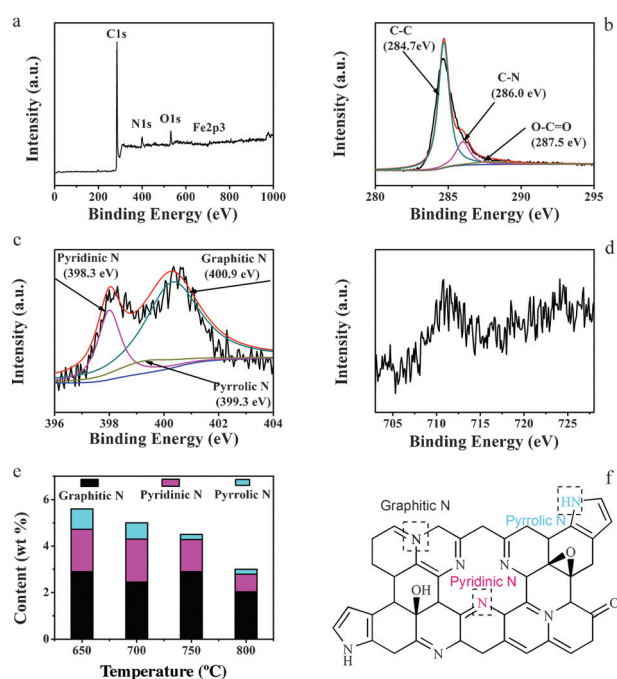

Figure 2. a) $Fe_3C/C-N_{750}$ NPs with core-shell structures and sheet-like carbon; b) Magnification image of a single particle; c) HRTEM image of a particle; d) HADDF-STEM image of $Fe_3C/C-N_{750}$ NPs; and e–h) the elemental mapping for the box region in (d).

resents an enlarged image of an isolated encapsulated particle. The image clearly indicates that the quasi-spherical particle has a core-shell structure with a complete and tight encapsulation. Figure 2c shows a HRTEM image of a $Fe_3C/C-N_{750}$ particle. It is seen that the lattice fringes are 0.21 and 0.34 nm, which are attributed to an interplanar spacing of graphite (002) and Fe_3C (211) crystal plane, respectively. The high angle annular dark-field scanning TEM (HAADF-STEM, in Figure 2d) reveals the positions of sheet-like carbon and the core-shell structure nature of $Fe_3C/C-N_{750}$ NPs. The elemental mapping results (Figure 2e–h) demonstrate the uniform distribution of C, Fe, and N. Importantly, N is detected over the whole area, which may be in favor of improving ORR performance of the materials.[21]

Based on all of the above analysis, a possible mechanism for the formation of $Fe_3C/C-N_x$ NPs is proposed. First, when the aniline is added to the mixture of $FeCl_3$ and AN, part of it will be converted into nitrobenzene, quinoid, or/and oligomers of aniline and so on immediately. Then the rest of aniline and AN will provide electrons to Fe^{3+} ions to form an iron–aniline–AN coordination structure. It is assumed that the $[Fe(aniline)_x(AN)_{6-x}]Cl_3$ is the most possible one. During the water bath process, some AN may evaporate, leading to a stronger interaction between the Fe^{3+} ions and nitrogen atoms. By increasing the calcination temperature, quinoid, or/and oligomers of aniline are decomposed to form a complicated carbon matrix. The $[Fe(aniline)_x(AN)_{6-x}]Cl_3$ part is simultaneously transformed

Figure 3. a) Low-resolution XPS spectrum for $Fe_3C/C-N_{750}$ NPs, and high-resolution b) C 1s; c) N 1s; and d) Fe 2p XPS spectra for $Fe_3C/C-N_{750}$ NPs; e) Concentrations of the three types of nitrogen in $Fe_3C/C-N_x$ samples obtained at different temperatures; f) Illustration of three types of nitrogen in grapheme.[22]

these elements in the samples. The concentrations of the N and Fe in each sample are demonstrated in Table S1 (the Supporting Information). It is shown that pyrolysis treatments at elevated temperatures (650–800 °C) lead to a significant decrease of Fe and N. Figure 3b depicts the high-resolution C 1s spectrum of $Fe_3C/C-N_{750}$ NPs. It is deconvoluted into three peaks at 284.7, 286.0, and 287.5 eV, which are consistent with C—C, C—N, and O—C=O, respectively, signifying that a high degree of graphitization of this sample. In Figure 3c, the N 1s spectrum can be deconvoluted into three peaks at 398.3, 399.3, and 400.9 eV, which are assigned to pyridinic-N, pyrrolic-N, and graphitic-N as illustrated in Figure 3f, signifying that ni-

trogen is indeed doped into the materials.[23] It should be noted that pyridinic and pyrrolic-N can combine with Fe to form the Fe-N_x moieties, and researchers believe that the pyridinic-N and graphitic-N are beneficial for ORR. Furthermore, according to the integrated peak areas, we quantify the concentrations of the three kinds of nitrogen, as shown in Table S1 (the Supporting Information). It can be seen that graphitic-N is the dominated species in all samples (Figure 3e), and Fe_3C/C-N_{750} NPs possesses the highest concentration of graphitic-N among the series, which reaches 2.9 at%. It also can be seen that the concentration of pyridinic-N and pyrrolic-N are much lower in all samples. With increasing the calcination temperature, the concentration of pyridinic-N and pyrrolic-N are decreased markedly, indicating that the thermal stability of pyridinic-N and pyrrolic-N are weaker than that of graphitic-N. Furthermore, in Figure 3d, there is a negligible surface iron content on the Fe_3C/C-N_{750} NPs from the high-resolution Fe 2p spectrum, which is likely because the Fe_3C NPs are encased exclusively by the graphite carbon.

Magnetic properties

Magnetic measurements (Figure 4a) reveal that all of the as-synthesized Fe_3C/C-N_x NPs display soft magnetic properties, and the Fe_3C/C-N_{800} NPs has the highest M_s value of 77.2 emu g^{-1} compared with those of its high-temperature annealed counterparts. The inset picture in Figure 4a demon-
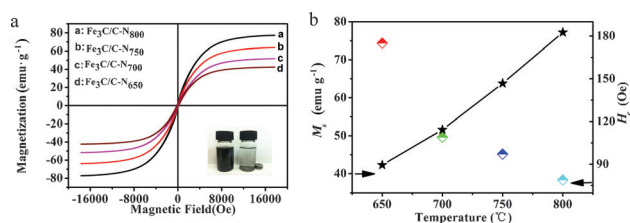

Figure 4. a) *M*–*H* plots of the as-synthesized Fe_3C/C-N_x NPs; b) The graph of the M_s and H_c versus calcination temperature.

strates that the materials can be easily recovered from suspensions. The M_s and H_c values versus calcinations temperature are summarized in Figure 4b. One can see that the M_s values tend to increase upon increasing the calcinnation temperature, which is due to the different crystallite sizes of the samples. In contrast, the coercivity (H_c) values decrease from 175 to 78.9 Oe. The detailed magnetic data of the four Fe_3C/C-N_x NPs are shown in Table S2 (the Supporting Information).

In this work, it is believed that the magnetic properties relate closely to the electrochemical properties of the materials. As we all know, all of the magnetic nanomaterials possess the magnetocrystalline anisotropy which is caused by two main reasons: 1) the combined effect of crystalline field and spin-orbit interaction; 2) the effect of spin-orbit interaction to the energy band. When the M_s values increase, the magnetocrystalline anisotropy will decrease. The π electronics that belong to the carbon shell tend to combine with the unoccu-

pied orbital of the magnetic (Fe_3C) core easily, leading to the enhanced electrochemical properties of the magnetic materials.

Electrochemical properties

Further, the as-synthesized Fe_3C/C-N_x NPs are used as electrocatalysts for the ORR. The cyclic voltammetry (CV) and rotating ring-disk electrode (RRDE) techniques are used to analyze their electrocatalytic performance. Figure 5 depicts the CV curves of the as-synthesized Fe_3C/C-N_x NPs that are obtained in a 0.1 M
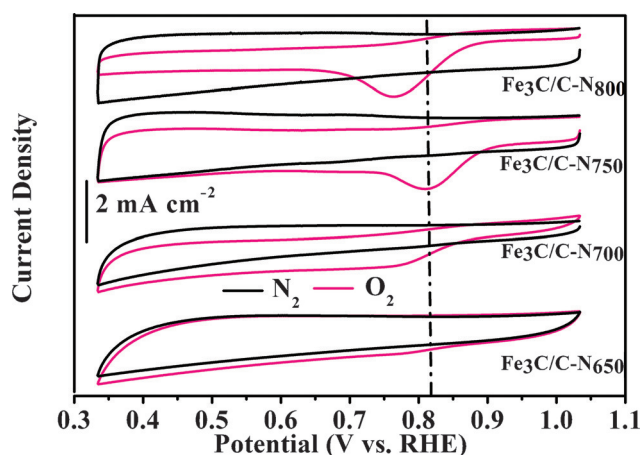

Figure 5. CV curves of Fe_3C/C-N_{650}, Fe_3C/C-N_{700}, Fe_3C/C-N_{750}, and Fe_3C/C-N_{800} NPs in N_2-saturated, O_2-saturated 0.1 M KOH solution at a scan rate of 10 mV s^{-1}.

KOH solution saturated with N_2 or O_2 at the scan rate of 10 mV s^{-1}. One can see that there are quasi-rectangular voltammograms without redox peaks for all the four samples when the electrolyte is saturated with N_2. However, when the O_2 is involved, an obvious ORR peak is observed, signifying that these materials are sensitive toward ORR. Among the series, Fe_3C/C-N_{750} shows the most positive peak potential of 0.82 V, suggesting that Fe_3C/C-N_{750} has a highly pronounced ORR activity compared with those of its high-temperature annealed counterparts. Note that, the Fe_3C/C-N_{750} sample possesses the highest concentration of graphitic-N among the series (Figure 3e and Table S1, the Supporting Information), signifying that graphitic-N likely plays a dominant role in the determination of the ORR activity.

Figure 6a shows the typical RRDE voltammograms of Fe_3C/C-N_{750} and commercial Pt/C catalyst obtained at room temperature in O_2-saturated 0.10 M KOH solution. Fe_3C/C-N_{750} NPs shows a higher electrocatalytic activity towards ORR than commercial Pt/C catalyst, as indicated by its 30 mV more positive half-wave potential ($E_{1/2}$) compared with that of the commercial Pt/C catalyst. Moreover, the onset potential is identified at +0.99 V for the Fe_3C/C-N_{750} and +0.98 V for the commercial Pt/C; these values are more positive than the Fe–C–N catalysts that were prepared by complex methods in recent studies.
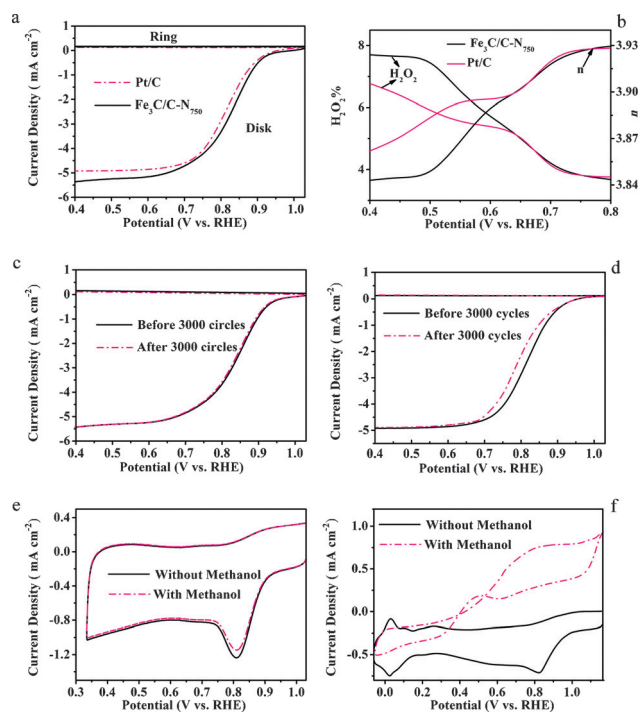
Figure 6. a) RRDE voltammograms; b) Plots of H_2O_2 yield and number of electron transfer of Fe$_3$C/C-N$_{750}$ and Pt/C at the rotation rate of 1600 rpm. LSV curves of c) Fe$_3$C/C-N$_{750}$, and d) Pt/C for ORR before and after 3000 cycles. CV curves of e) Fe$_3$C/C-N$_{750}$, and f) Pt/C without and with 1.0 M CH$_3$OH. All of these experiments were carried out in O$_2$-saturated 0.10 M KOH solution.

From the RRDE test, it can also be calculated that the H_2O_2 percent yield (H_2O_2%) and the number of electron transfer (n) involved in ORR by using the following Equations (1) and (2):

$$H_2O_2\ \% = \frac{200\,I_{Ring}/N}{I_{Ring}/N + I_{Disk}} \tag{1}$$

$$n = \frac{4\,I_{Disk}}{I_{Ring}/N + I_{Disk}} \tag{2}$$

in which N is the collection efficiency, I_{Disk} is the voltammetric currents at the risk electrode and I_{Ring} is the voltammetric currents at the ring electrode. In Figure 6b, it can be clearly seen that the yield of H_2O_2 for Fe$_3$C/C-N$_{750}$ is below 8.0% at all potentials, corresponding to an average n of 3.93, close to that of the Pt/C catalyst. To evaluate the durability of Fe$_3$C/C-N$_{750}$ in alkaline solution for the ORR, linear sweeps between 0.4 and 1.04 V are applied.

In Figure 6c, it can be seen that there is a slight ORR polarization curve shift after 3000 cycles for Fe$_3$C/C-N$_{750}$ sample, whereas a significant ORR polarization curve shift is observed for commercial Pt/C catalyst as shown in Figure 6d. In addition, the resistance of the Fe$_3$C/C-N$_{750}$ sample and Pt/C catalyst toward methanol crossover is also investigated. As shown in Figure 6e, after the addition of 1 M methanol to 0.10 M KOH electrolyte solution, no significant change is observed in the ORR current for the Fe$_3$C/C-N$_{750}$ sample. In contrast, there is

a significant change in the CV curve for the commercial Pt/C after methanol is added. These results confirm that the Fe$_3$C/C-N$_{750}$ sample exhibits stronger tolerance against methanol crossover than commercial Pt/C catalysts.

Moreover, the Fe$_3$C/C-N$_{750}$ catalyst also exhibits excellent ORR activity and stability in acidic solution as shown in Figure S3 (the Supporting Information). The onset potential is identified at $+0.82$ V for the Fe$_3$C/C-N$_{750}$, close to the $+0.91$ V for the commercial Pt/C catalyst. The H_2O_2% for Fe$_3$C/C-N$_{750}$ is below 5%, corresponding to an average n of 3.84. The stability of Fe$_3$C/C-N$_{750}$ is better than Pt/C catalyst as shown in Figure S3c and d (the Supporting Information).

Based on the structure, morphology, and composition of Fe$_3$C/C-N$_{750}$ NPs, it is believed that three important aspects should be responsible for its excellent ORR activity and stability: 1) Owing to the core-shell structure of the Fe$_3$C/C-N$_{750}$ NPs, there may be a host–guest electronic interaction between Fe$_3$C core and graphite carbon shell, making the outer surface of shell more active toward ORR;[24] 2) There may be a synergetic effect between sheet-like carbon and the encapsulated Fe$_3$C, which relates closely to the ORR activity and stability of the Fe$_3$C/C-N$_{750}$ NPs;[25] 3) The high percentage of graphitic-N (2.9 at.%) in the Fe$_3$C/C-N$_{750}$ NPs can lead to the charge delocalization, thus facilitating the bridge model chemisorption of O$_2$ on the Fe$_3$C/C-N$_{750}$ NPs, which can effectively weaken the O—O bonding to promote the ORR.[22]

Conclusions

A series of Fe$_3$C/C-N$_x$ NPs with different nitrogen contents was prepared by a simple one-pot route. In the synthetic procedure, aniline and AN are used as the carbon and nitrogen source. It is believed that an iron–aniline–AN coordination structure is involved in the nucleation process of Fe$_3$C. The effect of calcination temperature on the structural and functional properties of the materials is investigated. Magnetic measurements reveal that all of the as-prepared Fe$_3$C/C-N$_x$ NPs display ferrimagnetic behavior at room temperature, with the highest M_s value of 77.2 emu g^{-1} for Fe$_3$C/C-N$_{800}$ NPs. All of the as-prepared Fe$_3$C/C-N$_x$ NPs are also applied as the ORR catalysts. As a result, the Fe$_3$C/C-N$_{750}$ NPs emerges as a superior ORR electrocatalyst with highly pronounced electrocatalytic performance, long durability, high selectivity, and strong tolerance against methanol crossover. These characteristics are most likely due to the high percentage of graphitic-N and the unique structure of the Fe$_3$C/C-N$_{750}$ NPs. The findings of the synthetic route, the prepared materials of the unique structure, and the proposed mechanism paves a way to further development of active and durable ORR catalysts for fuel cell applications.

Experimental Section

Preparation of Fe$_3$C/C-N$_x$ NPs

The preparation process is depicted in Scheme 1. Firstly, FeCl$_3$ (0.02 mol) was added into acetonitrile (AN) (0.2 mol) with stirring.
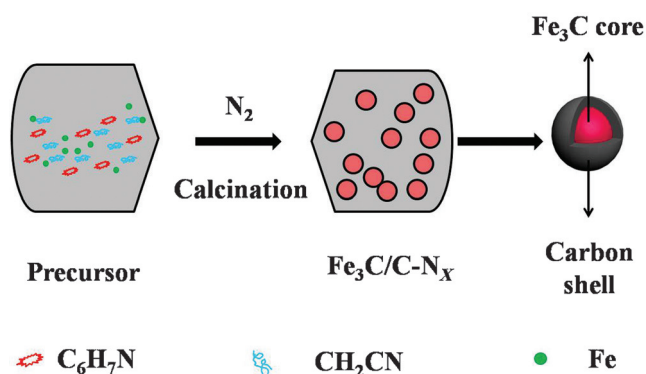
Scheme 1. Illustration of the preparation of the $Fe_3C/C-N_x$ NPs.

After 5 min, aniline (0.3 mol) was slowly added into above solution. The color of the solution gradually changed from yellow to dark brown. Subsequently, the mixture was transferred to an 80 °C water bath for 3 h. During this process, the mixture became viscous. Finally, the viscous mixture was calcinated at controlled temperatures (650, 700, 750, or 800 °C) for 2 h in a N_2 atmosphere at the gas flow rate of 320 sccm.

Characterizations

The X-ray powder diffraction (XRD) patterns were recorded on a Shimadzu XRD-6100 using $Cu_{K\alpha}$ radiation ($\lambda = 0.15405$ nm). Raman spectra were measured with a JobinYvon/HORIBA LabRam ARAMIS Raman spectrometer with the radiation from an air-cooled He Ne laser (633 nm). The Brunauer–Emmet–Teller (BET) surface area was determined by using a Micromeritics ASAP 2020 instrument at 77 K. The Fourier Transform Infrared (FTIR) Spectrometer spectrum was recorded on a Shimadzu IRAffinity-1 FTIR spectrometer using KBr pellets in the wavenumber range of 4000–400 cm^{-1}. Thermogravimetric analysis (TGA) was carried out using a Rheometric Scientific DSC QC (TA, USA) under a N_2 atmosphere at a heating rate of 5 °C min^{-1}. High-resolution transmission electron microscopy (HRTEM) images were obtained with a Philips Tecnai G2 F20 High Resolution Transmission Electron Microscopy equipped with an EDS detector at an acceleration voltage of 100 kV. The magnetic properties were determined by using a LakeShore 7404 vibrating sample magnetometer (VSM) in the magnetic field of $-17\,000$ to $+17\,000$ Oe. Finally, the X-ray Photoelectron Spectroscopy (XPS) spectra were recorded using an ESCALAB 250 spectrometer with a mono X-ray source $Al_{K\alpha}$ excitation (1486.6 eV).

Electrochemical measurement

Electrochemical measurements were performed in a standard three-electrode system controlled by a CHI 760D electrochemistry workstation (CH Instruments, Chenhua Co., China). A platinum wire was used as the counter electrode, an Ag/AgCl as the reference electrode, and a catalyst-modified glassy carbon electrode (GCE) as the working electrode. The catalyst ink was prepared by adding 10 mg of catalyst into a mixture of deionized water, isopropyl alcohol, and Nafion (5.0 wt %) at a volume ratio of 20:1:0.075 to form a homogeneous suspension at the catalyst concentration of 2 mg mL^{-1}. The GCE was polished carefully to a mirror finish by using the 0.3 μm alumina slurries. After that, the GCE was sonicated in acetone, ethanol and deionized water successively to remove any bound particles, and dried under a gentle air stream. Then, a certain amount of the catalyst ink was evenly casted onto the

pretreated GCE surface with a loading amount of 1.5 mg cm^{-2}. Finally, the modified electrodes were then dried under ambient conditions for electrochemical measurements. As a comparison, the commercial Pt/C catalyst was prepared according to the same procedure. Linear sweep voltammograms (LSV) were acquired in an O_2-saturated 0.1 M KOH solution and 0.1 M HClO$_4$ solution at a rotation rate of 1600 rpm. In the measurements, the Ag/AgCl reference electrode was calibrated with respect to a reversible hydrogen electrode (RHE).

[1] a) M. K. Debe, *Nature* **2012**, *486*, 43–51; b) B. C. Steele, A. Heinzel, *Nature* **2001**, *414*, 345–352.

[2] a) Y.-J. Wang, N. Zhao, B. Fang, H. Li, X. T. Bi, H. Wang, *Chem. Rev.* **2015**, *115*, 3433–3467; b) A. Chen, P. Holt-Hindle, *Chem. Rev.* **2010**, *110*, 3767–3804; c) S. E. Kleijn, S. Lai, M. Koper, P. R. Unwin, *Angew. Chem. Int. Ed.* **2014**, *53*, 3558–3586; *Angew. Chem.* **2014**, *126*, 3630–3660; d) C. Wang, H. Daimon, Y. Lee, J. Kim, S. Sun, *J. Am. Chem. Soc.* **2007**, *129*, 6974–6975; e) S. Guo, S. Zhang, S. Sun, *Angew. Chem. Int. Ed.* **2013**, *52*, 8526–8544; *Angew. Chem.* **2013**, *125*, 8686–8705; f) S. Sun, Z. Jusys, R. J. Behm, *J. Power Sources* **2013**, *231*, 122–133; g) X. Zhou, Y. Gan, J. Du, D. Tian, R. Zhang, C. Yang, Z. Dai, *J. Power Sources* **2013**, *232*, 310–322.

[3] a) X. Zhao, S. Chen, Z. Fang, J. Ding, W. Sang, Y. Wang, J. Zhao, Z. Peng, J. Zeng, *J. Am. Chem. Soc.* **2015**, *137*, 2804–2807; b) W. Wang, Y. Zhao, Y. Ding, *Nanoscale* **2015**, *7*, 11934–11939.

[4] W. Xia, J. Masa, M. Bron, W. Schuhmann, M. Muhler, *Electrochem. Commun.* **2011**, *13*, 593–596.

[5] a) F. Jaouen, E. Proietti, M. Lefèvre, R. Chenitz, J.-P. Dodelet, G. Wu, H. T. Chung, C. M. Johnston, P. Zelenay, *Energy Environ. Sci.* **2011**, *4*, 114–130; b) Z. Chen, D. Higgins, A. Yu, L. Zhang, J. Zhang, *Energy Environ. Sci.* **2011**, *4*, 3167–3192; c) H. Yuan, Y. Hou, Z. Wen, X. Guo, J. Chen, Z. He, *ACS Appl. Mater. Interfaces* **2015**, *7*, 18672–18678.

[6] a) G. Wu, K. L. More, C. M. Johnston, P. Zelenay, *Science* **2011**, *332*, 443–447; b) Y. Hu, J. O. Jensen, W. Zhang, S. Martin, R. Chenitz, C. Pan, W. Xing, N. J. Bjerrum, Q. Li, *J. Mater. Chem. A* **2015**, *3*, 1752–1760; c) J. Wang, G. Wang, S. Miao, X. Jiang, J. Li, X. Bao, *Carbon* **2014**, *75*, 381–389; d) S. Chao, Q. Cui, K. Wang, Z. Bai, L. Yang, J. Qiao, *J. Power Sources* **2015**, *288*, 128–135; e) A. Muthukrishnan, Y. Nabae, C. W. Chang, T. Okajima, T. Ohsaka, *Catal. Sci. Technol.* **2015**, *5*, 1764–1774.

[7] a) N. Daems, X. Sheng, I. F. J. Vankelecom, P. P. Pescarmona, *J. Mater. Chem. A* **2014**, *2*, 4085–4110; b) Q. Li, H. Pan, D. Higgins, R. Cao, G. Zhang, H. Lv, K. Wu, J. Cho, G. Wu, *Small* **2015**, *11*, 1443–1452; c) W.-B. Luo, S.-L. Chou, J.-Z. Wang, Y.-C. Zhai, H.-K. Liu, *Small* **2015**, *11*, 2817–2824; d) A. Zehtab Yazdi, K. Chizari, A. S. Jalilov, J. Tour, U. Sundararaj, *ACS Nano* **2015**, *9*, 5833–5845.

[8] a) M. Kim, D.-H. Nam, H.-Y. Park, C. Kwon, S. Yoo, J. Jang, H.-J. Kim, E. Cho, H. Kwon, *J. Mater. Chem. A* **2015**, *3*, 14284–14290; b) Z. Lu, G. Xu, C. He, T. Wang, L. Yang, Z. Yang, D. Ma, *Carbon* **2015**, *84*, 500–508; c) M. Li, X. Bo, Y. Zhang, C. Han, A. Nsabimana, L. Guo, *J. Mater. Chem. A* **2014**, *2*, 11672–11682.

[9] Y. Hou, T. Huang, Z. Wen, S. Mao, S. Cui, J. Chen, *Adv. Energy Mater.* **2014**, *4*, 1400337.

[10] W. Yang, X. Liu, X. Yue, J. Jia, S. Guo, *J. Am. Chem. Soc.* **2015**, *137*, 1436–1439.

[11] a) Y. Hu, J. O. Jensen, W. Zhang, L. N. Cleemann, W. Xing, N. J. Bjerrum, Q. Li, *Angew. Chem. Int. Ed.* **2014**, *53*, 3675–3679; *Angew. Chem.* **2014**, *126*, 3749–3753; b) G. Zhong, H. Wang, H. Yu, F. Peng, *J. Power Sources* **2015**, *286*, 495–503.

[12] S. Gao, K. Geng, H. Liu, X. Wei, M. Zhang, P. Wang, J. Wang, *Energy Environ. Sci.* **2015**, *8*, 221–229.

[13] a) G. Liu, X. Li, J.-W. Lee, B. N. Popov, *Catal. Sci. Technol.* **2011**, *1*, 207–217; b) X. Zhou, Z. Yang, H. Nie, Z. Yao, L. Zhang, S. Huang, *J. Power Sources* **2011**, *196*, 9970–9974.

[14] F. Tuinstra, J. L. Koenig, *J. Chem. Phys.* **1970**, *53*, 1126–1130.

[15] X. Wang, P. Zhang, J. Gao, X. Chen, H. Yang, *Dyes Pigments* **2015**, *112*, 305–310.

[16] X. Wang, P. Zhang, W. Wang, X. Lei, B. Zou, H. Yang, *RSC Adv.* **2015**, *5*, 27857–27861.

[17] J. W. Chevalier, J. Y. Bergeron, L. H. Dao, *Macromolecules* **1992**, *25*, 3325–3331.

[18] M. I. Boyer, S. Quillard, E. Rebourt, G. Louarn, J. P. Buisson, A. Monkman, S. Lefrant, *J. Phys. Chem. B* **1998**, *102*, 7382–7392.

[19] Z. Schnepp, S. C. Wimbush, M. Antonietti, C. Giordano, *Chem. Mater.* **2010**, *22*, 5340–5344.

[20] W.-J. Liu, K. Tian, Y.-R. He, H. Jiang, H.-Q. Yu, *Environ. Sci. Technol.* **2014**, *48*, 13951–13959.

[21] W. Yang, X. Yue, X. Liu, J. Zhai, J. Jia, *Nanoscale* **2015**, *7*, 11956–11961.

[22] W. Niu, L. Li, X. Liu, N. Wang, J. Liu, W. Zhou, Z. Tang, S. Chen, *J. Am. Chem. Soc.* **2015**, *137*, 5555–5562.

[23] P. Chen, L.-K. Wang, G. Wang, M.-R. Gao, J. Ge, W.-J. Yuan, Y.-H. Shen, A.-J. Xie, S.-H. Yu, *Energy Environ. Sci.* **2014**, *7*, 4095–4103.

[24] a) X. Zheng, J. Deng, N. Wang, D. Deng, W. H. Zhang, X. Bao, C. Li, *Angew. Chem. Int. Ed.* **2014**, *53*, 7023–7027; *Angew. Chem.* **2014**, *126*, 7143–7147; b) H. T. Chung, J. H. Won, P. Zelenay, *Nat. Commun.* **2013**, *4*, 1922.

[25] Y. Hu, J. O. Jensen, W. Zhang, Y. Huang, L. N. Cleemann, W. Xing, N. J. Bjerrum, Q. Li, *ChemSusChem* **2014**, *7*, 2099–2103.